Nickel (II) Tetradentate Complexes Bearing NHC-Pyridyl Derived Ligands for Photocatalytic CO_2 Reduction to Formate and CO

Sonya Y. Manafe,[a] Gbolagade Olajide,[b] Chance M. Boudreaux,[a] Fengrui Qu,[a,c] Logan M. Whitt,[a] Patrick D. Pridemore,[a] James Fletcher Hall,[a] Tibor Szilvási,[b] and Elizabeth T. Papish[a]

[a]Department of Chemistry and Biochemistry, University of Alabama, Shelby Hall, Tuscaloosa, Alabama 35487, United States
[b] Department of Chemical and Biological Engineering, University of Alabama, Tuscaloosa, Alabama 35487, United States
[c]Department of Chemistry, University of Michigan, X-Ray Shop, Ann Arbor, Michigan 48109, United States

* Corresponding Authors

Email addresses:
tibor.szilvasi@ua.edu
etpapish@ua.edu

INTRODUCTION

The catalytic conversion of CO_2 into liquid fuels is of broad interest as it could potentially offset CO_2 emissions which contribute to climate change.[1-4] However, CO_2 is a stable molecule formed by the combustion of fossil fuels. Thus, appropriate catalysts and energy input are required for recycling CO_2 into other useful chemicals.[2, 3, 5] Photocatalytic CO_2 reduction to form HCO_2^- and CO is a viable method for fuel formation from a greenhouse gas form, and the resulting CO could be used to produce diesel fuels through the Fischer-Tropsch process. [6-8]

The development of visible-light photocatalytic system utilizing earth-abundant metals such as Ni and Co bearing multidentate NHC-type ligands for CO_2 reduction has been studied recently.[6, 9-12] In 2013, Chang and co-workers utilized nickel complexes with N-heterocyclic carbene-isoquinoline type ligands (e.g. **Lit-1**, **Figure 1**) as photocatalysts for the conversion of CO_2 to CO with high selectivity over proton reduction. In the presence of $Ir(ppy)_3$ as the photosensitizer, **Lit-1** (**Figure 1**) produced a high turnover number (TON) of CO 98,000 and a turnover frequency (TOF) of 3.9 s^{-1}.[9] Jurss and Delcamp reported nickel complexes bound to macrocyclic tetradentate bipyridyl-NHC ligands (e.g. **Lit-2**, **Figure 1**), which showed high selectivity for CO_2 reduction with 310,000 TON of CO (**Figure 1**).[10] Significantly, the addition of 2% v/v H_2O in this reaction produced CH_4 with 19,000 TON.

In 2017, Webster and Papish reported Ir complexes binding bidentate NHC-pyridinol-derived ligands (NHC-py^{OR}) as catalysts for aqueous CO_2 hydrogenation and formic acid dehydrogenation reactions (**Figure 1**, **Lit-3**). [9, 13] Inspired by Chang's work, this bidentate NHC-pyridinol type ligand can be modified to make tetradentate NCCN NHC-pyridyl derived ligands (**Figure 1**, right). In this study, three different substituents ortho to N on the pyridine ring (OMe, OBn and OH), and the unsubstituted NHC-pyridine ligand (R = H) reported by Chang's group in

2011[14] are used to investigate structure-function relationship of this ligand system in nickel(II) complexes as photocatalysts for CO_2 reduction to CO.

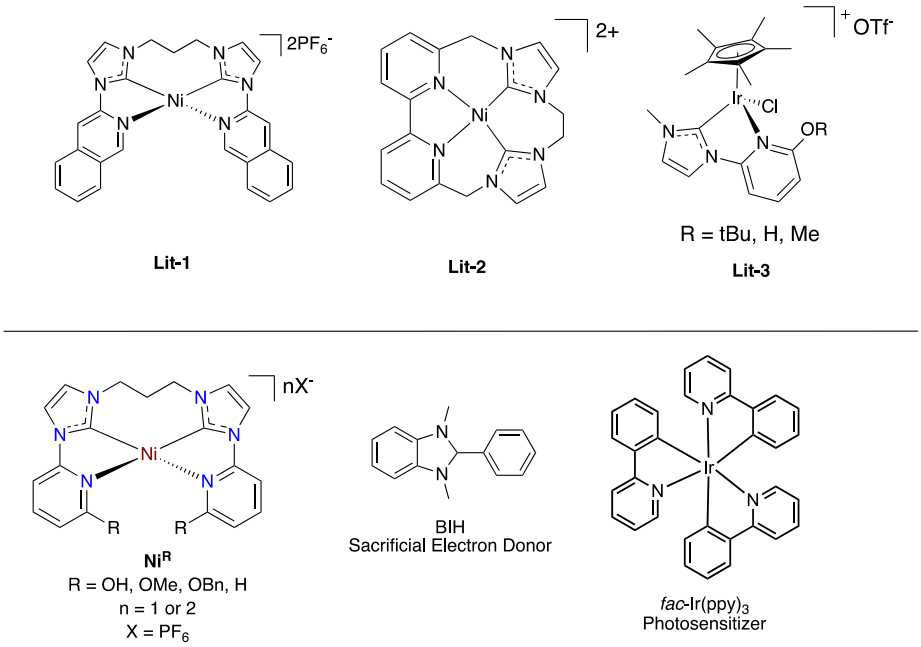

Figure 1: Catalysts used in the literatures (top); Ni-NCCN-type complexes, sacrificial electron donor, and photosensitizer used in this study (bottom).

RESULT AND DISCUSSION

Synthesis and Characterization

The new NCCN ligands were synthesized through the nucleophilic substitution of 2,6-difluoropyridine. The initial step of this synthesis route was adapted from the procedure in the literatures[13, 15] (**Scheme 1**). 1,3-dibromopropane was reacted with NaI in acetone via the Finkelstein substitution reaction to produce 1,3-diiodopropane. The resulting product, 1,3-diiodopropane, was then treated with compound $\mathbf{1^R}$ to undergo an S_N2 reaction in 120 °C of acetone to make compound $\mathbf{2^R}$. The product was precipitated out of the solution as a light-yellow solid after heating for 16 h. Compound $\mathbf{2^R}$ was then treated with aqueous KPF_6 to undergo a salt

metathesis reaction, which resulted in a white solid precipitate, $\mathbf{3^R}$. These carbene precursors were then metalated using silver(I) oxide in acetonitrile to produce the Ag-adducts, ($\mathbf{4^{OMe}}$ and $\mathbf{4^{OBn}}$) as greyish-white solids which were characterized by ^{1}H-NMR, FTIR, and HRMS.

The $\mathbf{Ni^R}$ complexes were synthesized by treating Ag-adducts ($\mathbf{4^{OMe}}$ and $\mathbf{4^{OBn}}$) with Ni(dme)Cl_2 (dme = dimethoxyethane) in acetonitrile at room temperature (**Scheme 1**). This results in an orange salt as the product for both complexes, in ~ 85% yield. Complexes $\mathbf{Ni^R}$ were characterized by ^{1}H-NMR, ^{19}F-NMR, FTIR, and HRMS. The aromatic peaks for both complexes are easily assigned in the ^{1}H-NMR, however, the proton peaks for N-methylene protons are broadened. This is probably due to the protons of the propyl chain being in different environments because of the multiple conformations being possible for the ring which results in small variations in the chemical shifts.

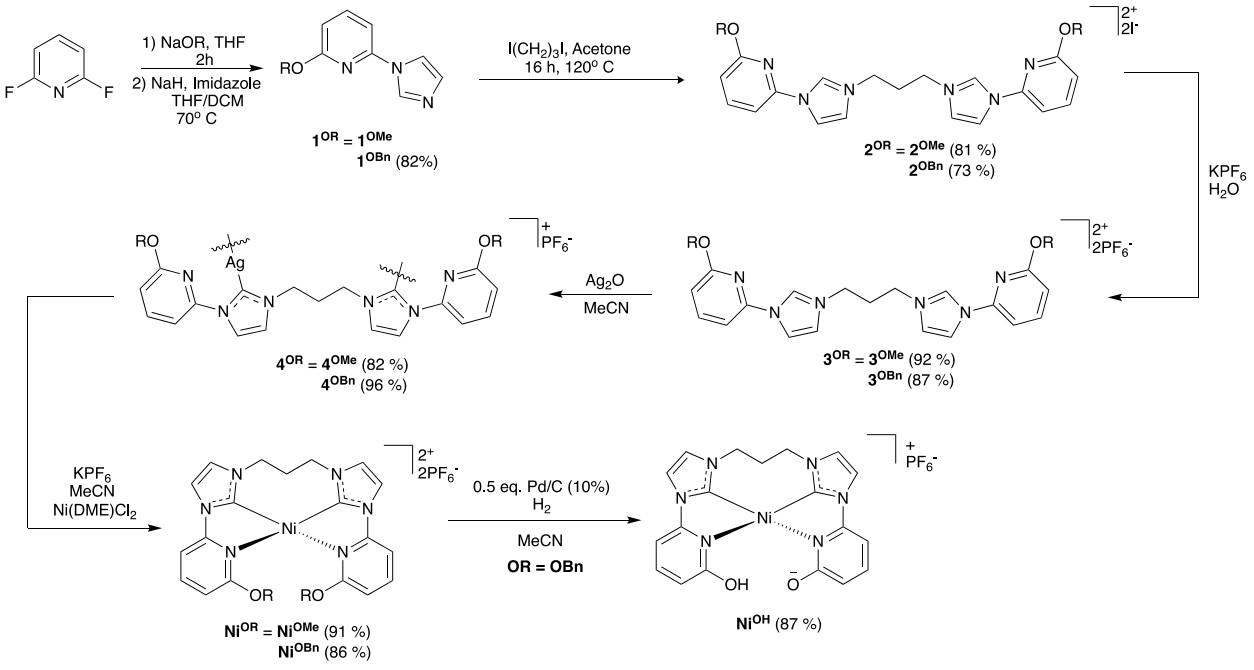

Scheme 1: Synthesis route of complex $\mathbf{Ni^{OR}}$

Complex **Ni^{OBn}** was targeted since the OBn protecting group is easily removed by hydrogenation to reveal the free pyridinol motif (**Ni^{OH}**). The hydrogenation reaction of **Ni^{OBn}** was conducted with 10% Pd/C and 1 atm of H_2 at room temperature in acetonitrile and produced an orange solid, **Ni^{OH}**, as the product in ~85% yield (**Scheme 1**). The loss of benzyl peaks in the ^{1}H-NMR (**Figure S32**) confirmed that the hydrogenation had occurred. Recrystallization of **Ni^{OH}** through the vapor diffusion method of diethyl ether into an acetonitrile solution produced an orange crystal that is suitable for the Single Crystal X-Ray Diffraction (SC-XRD). Crystallography analysis revealed that one of the OH group *ortho* to the N of the pyridine deprotonated *in situ* to produce an OH---O$^-$ structure (**Figure 2**, right), which is a mono-cation with one PF_6^- counter anion. A weak and broad stretching frequency between 2500 cm^{-1} and 3500 cm^{-1} is also observed in the FT-IR (**Figure S36**), confirming that there is an OH group in this **Ni^{OH}** complex.

Single Crystal X-Ray Diffraction

Crystals of **Ni^{OMe}** and **Ni^{OBn}** were grown from the slow evaporation of an acetonitrile solution, while **Ni^{OH}** was recrystallized by the vapor diffusion of diethyl ether into acetonitrile solution. The four-coordinate nickel centers for these three complexes are in a distorted seesaw geometry with the four-coordinate τ_4 and τ_4' indexes approximately equal to 0.3 (**Figure 2**).[16, 17] The τ_4 and τ_4' parameters estimate the distortion between square planar and tetrahedral with 1.00, representing a perfect tetrahedral geometry, 0 representing a perfect square planar geometry. The intermediate structures such as trigonal pyramidal and seesaw can have intermediate τ_4 and τ_4' values (e.g. 0.5). The calculation of τ_4 and τ_4' values involve the largest angles around the metal center, however α and β are treated differently in τ_4' that makes distortions away from ideal tetrahedral geometry more obvious.[18] The resulting OH group from the hydrogenation of OBn

group is acidic, and readily loses a proton to form an OH---O^- bridging hydrogen bonding interaction that closes the ligand macrocycle. The O---O distance within the O···H···O hydrogen bonding interaction is 2.401 (2) Å which indicates a moderately strong hydrogen bond. The angle between two planes ($\angle N_{Py} - Ni - C_{NHC}$) formed from each half of the ligand around Ni center was measured to explain the distortion towards square planar geometry. The angle of all three complexes (**Ni^{OMe}**, **Ni^{OBn}**, and **Ni^{OH}**) are in the range of 33.0° to 35.0° (**Figure 2**), which is slightly larger than that of the equivalent unsubstituted structure reported by Chang et al., which was 31.0°.[14] The increased angle in the substituted structure is mainly attributed to the steric repulsion of the substituents. The average C–O bond distance between carbon ortho to N or pyridine and oxygen of the substituents group for **Ni^{OMe}** and **Ni^{OBn}** are identical with 1.334 (2) Å and. 1.334 (1) Å, respectively, meanwhile the average C–O bond distance of **Ni^{OH}** is slightly shorter than the other two Ni(II) complexes, with 1.298 (3) Å. This is probably due to the charge different in **Ni^{OH}**, as the deprotonated hydroxyl group gives a negative charge on the oxygen (OH---O^-), causing the pyridine ring to be partially dearomatized. Moreover, the C2 – C3 bond distances of **Ni^{OMe}** and **Ni^{OBn}** are also identical with 1.398 (2) Å and 1.399 (2) Å, respectively, while the bond distance of C2 – C3 for **Ni^{OH}** is slightly longer, with 1.412 (2) Å. Overall, the other bonds distances, angles, and geometry of each complex are approximately in the same range without significant changes (**Table 1**).

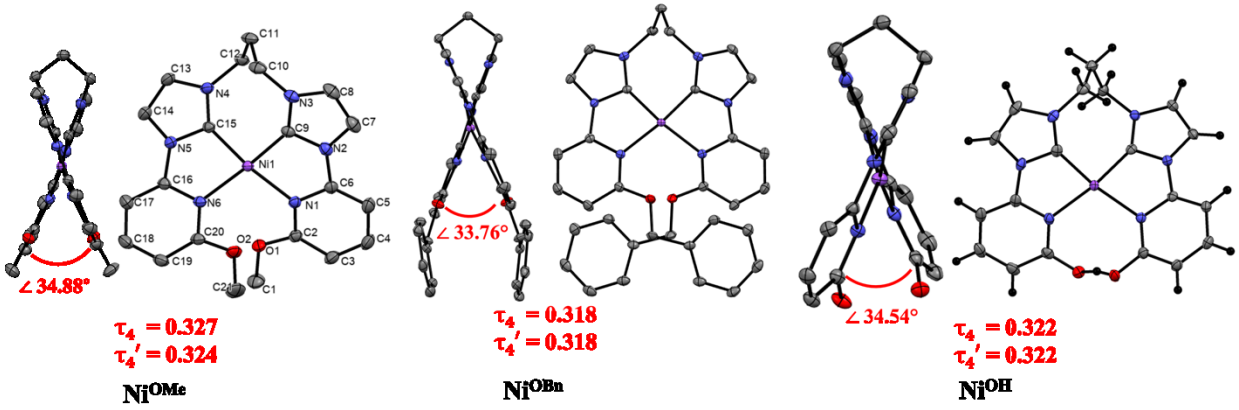

Figure 2: ORTEP top and side view diagrams of $\mathbf{Ni^{OMe}}$ (left), $\mathbf{Ni^{OBn}}$ (middle), and $\mathbf{Ni^{OH}}$ (right) based on crystallographic data with hydrogen atoms and anions removed for clarity. Thermal ellipsoids are drawn at 50% probability level.

Table 1: Selected bond lengths, angles, τ_4, and τ_4' parameter for Ni(II)-NCCN complexes.

Designation	$\mathbf{Ni^{OMe}}$	$\mathbf{Ni^{OBn}}$	$\mathbf{Ni^{OH}}$	$\mathbf{Ni^{H[a]}}$
Bond Angle (°)				
N-Ni-C_{NHC}	**82.35 (4)**	**82.06 (4)**	**81.27 (6)**	**82.79 (10)**
	156.42 (5)	**157.61 (5)**	**157.28 (6)**	**157.99 (10)**
N-Ni-N	**105.89 (4)**	**106.28 (5)**	**110.36 (7)**	**103.39 (9)**
C-Ni-C	**98.54 (5)**	**98.08 (7)**	**95.13 (9)**	**98.13 (11)**
τ_4 parameter	**0.327**	**0.318**	**0.322**	**0.291**
τ_4' parameter	**0.324**	**0.318**	**0.322**	**0.281**
Two Planes Angles (°) ∠N_{Py} – Ni – C_{NHC}	**34.88**	**33.76**	**34.58**	**31.0**
Bond Lengths (Å)				
Ni-C_{NHC} (avg)	**1.848 (1)**	**1.859 (16)**	**1.859 (23)**	**1.855 (4)**
Ni-N_{py} (avg)	**1.961 (9)**	**1.982 (13)**	**2.042 (20)**	**1.956 (3)**
C_{py}-O (avg)	**1.334 (2)**	**1.334 (1)**	**1.298 (3)**	**n/a**

Averages are used when applicable. [a]These numbers are from the literature.[14]

UV-Visible Absorption Spectroscopy

UV-Visible spectroscopy studies were performed to investigate the electronic influence of Ni complexes bearing NCCN-type ligands (**Figure 4**). All nickel complexes show two major energy absorption peaks above 250 nm. The high energy absorption peaks for $\mathbf{Ni^{OMe}}$ and $\mathbf{Ni^{OBn}}$ are at 296 nm and 295 nm, respectively, with the extinction coefficient (ε) around 13,000 to 14,000 $M^{-1}cm^{-1}$ for both complexes (**Table 2**, **Figure S35 & S39**). Meanwhile the high energy absorption peaks for $\mathbf{Ni^{OH}}$ and $\mathbf{Ni^{H}}$ are of lower intensity compared to $\mathbf{Ni^{OMe}}$ and $\mathbf{Ni^{OBn}}$. Interestingly, $\mathbf{Ni^{OH}}$ has a longer shoulder wavelength at 305 nm with an extinction coefficient of 6,000 ± 60 $M^{-1}cm^{-1}$ (**Table 2**, **Figure S43**). These peaks are assigned to π to π* transitions (**Table S3**).

Moderately intense peaks at 320 nm to 365 nm were observed for three nickel complexes, ($\mathbf{Ni^{OMe}}$, $\mathbf{Ni^{OBn}}$, and $\mathbf{Ni^{OH}}$) with extinction coefficient (ε) varying from 3,000 to 6,000 $M^{-1}cm^{-1}$ for all three complexes (**Table 2**). On the other hand, the unsubstituted Ni-NCCN complex, $\mathbf{Ni^{H}}$, has its absorption peaks at 277 nm and 344 nm with extinction coefficient of 4,800 ± 90 $M^{-1}cm^{-1}$ and 2,000 ± 30 $M^{-1}cm^{-1}$, respectively (**Table 2**, **Figure S48 – S49**). Lastly, weak bands are observed for complexes $\mathbf{Ni^{OMe}}$, $\mathbf{Ni^{OBn}}$, and $\mathbf{Ni^{OH}}$ at above 400 nm (inset, **Figure 4**), with extinction coefficient (ε) varies from 400 $M^{-1}cm^{-}$ to 460 $M^{-1}cm^{-1}$ (**Table 2**, **Figure S37, S41, & S46**).

To investigate the transition character of the complexes, we performed density functional theory (DFT) calculations. We found that the calculated absorption energy is in good agreement with the experimental data (**Table S2**) with a mean absolute average error of 13 nm. The results of the Natural Transition Orbital (NTO) analysis (**Table 2** and **Table S3**) reveal that the absorption peaks at 277 nm and 344 nm for Ni^{H} correspond to MLCT transitions, and the absorption peaks at 321 nm, 363 nm, and 438 nm for Ni^{OH} also correspond to MLCT transitions. On the other hand, for Ni^{OMe}, the absorption peak at 296 nm corresponds to a π to π* transition, while the absorption

peaks at 360 nm and 454 nm correspond to MLCT transitions. For Ni^{OBn}, the absorption peak at 295 nm corresponds to a π to π* transition, while the absorption peaks at 365 nm and 460 nm correspond to MLCT transitions.

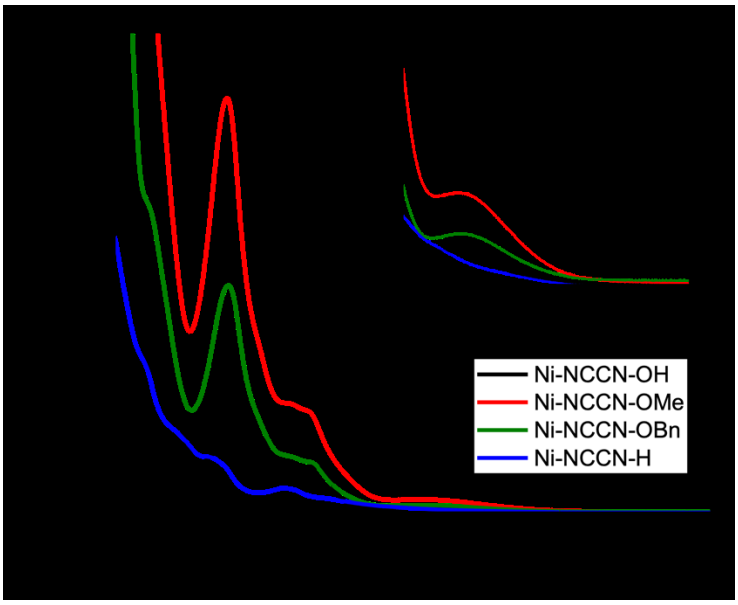

Figure 4: UV-Vis absorption spectra of **Ni^{OMe}**, **Ni^{OBn}**, **Ni^{OH}**, and **Ni^{H}** complexes in acetonitrile. The inset shows an expansion of the region above 400 nm.

Table 2: UV-Visible absorption features of Ni-NCCN type complexes

Complex	λ_{max} (nm)	Character	ε $(M^{-1}cm^{-1})$
[a]**Ni^{OMe}**	296	π to π*	13,200 ± 1000
	360	MLCT	3,400 ± 300
	454	MLCT	450 ± 70
[a]**Ni^{OBn}**	295	π to π*	13,800 ± 1700
	365	MLCT	3,000 ± 400
	460	MLCT	400 ± 10
Ni^{OH}	305[b]; 321	MLCT	6,000 ± 60
	363	MLCT	3,700 ± 20
	438	MLCT	400 ± 10

Ni^{H}	277	MLCT	4,800 ± 90
	344	MLCT	2,000 ± 30

[a]$\boldsymbol{\varepsilon}$ values are the average of 2 – 3 experiments; [b]Shoulder peak.

Electrochemical Study

The cyclic voltammetry (CV) experiments were conducted for two of the Ni(II) complexes, **Ni^{OMe}** and **Ni^{OH}**, to evaluate the redox properties of these complexes. The CV experiment of **Ni^{OBn}** was not done, as this complex was originally synthesized as a protecting group to synthesize **Ni^{OH}** ; on the other hand, the CV of **Ni^{H}** has already been reported in the literature.[14] The experiment was done under N_2 atmosphere with 1 mM of analyte and 100 mM of tetrabutylammonium hexafluorophosphate in acetonitrile solution, with scan rate of 100 mV/s. As shown in **Figure 5,** complex **Ni^{OMe}** displays two reduction peaks at -1.23 V, and -1.93 V vs. Fc^+/Fc. The third reduction potential of this **Ni^{OMe}** compound was observed at -2.10 V vs. Fc^+/Fc at higher scan rate (**Figure S50**). The CV experiment was repeated under CO_2 atmosphere to investigate the ability of this complex to electrochemically reduce CO_2. Two irreversible reduction peaks were shown at -1.23 V and -1.79 V vs. Fc^+/Fc. The first reduction peaks under both N_2 and CO_2 condition are quasi reversible with peak-to-peak splitting (ΔE_P) of 73 and 74 mV, respectively, at a scan rate of 100 mV/s. Another Ni-NCCN complex with more electron donating group, **Ni^{OH}**, also exhibits two irreversible reduction peaks under N_2 atmosphere at -1.44 V, and -2.18 V vs Fc^+/Fc. The other reduction potential at 1.90 V appeared at the scan rates of 150 to 250 mV/s (**Figure S52**) but it is not obvious at a scan rate of 100 mV/s. Under CO_2 atmosphere, **Ni^{OH}** shows two reduction peaks at -1.45 V and -2.10 V vs Fc^+/Fc. The first reduction peak of **Ni^{OH}** is quasi-reversible with peak-to-peak splitting (ΔE_P) of 52 mV at a scan rate of 100 mV/s. The reduction potential peaks for **Ni^{OH}** under CO_2 and N_2 are slightly more negative compared to the potential peaks for **Ni^{OMe}.**

Interestingly, there is no significant increase in the current of these two nickel complexes under CO_2 atmosphere as the i_{cat}/i_p value is ≤ 1 (**Table 3**). Thus, water was introduced to the solution as a proton source to promote the proton-coupled reduction of CO_2.[5] Upon the addition of water, a considerable current enhancement was observed for both nickel complexes, under CO_2 atmosphere relative to the anhydrous acetonitrile solution (**Figure 5**). However, the i_{cat}/i_p value is still less than 2.0 for both complexes (**Table 3**). Another proton source such as phenol was also used for the CV of **Ni^{OMe}**. Interestingly, the addition of phenol to the solution gives the same current enhancement as observed in the addition of water. Thus, these Ni-NCCN type complexes might not be good electrocatalysts for CO_2 reduction under aprotic conditions but can still activate the CO_2 with small i_{cat}/i_p values with additional proton sources. The cyclic voltammogram of **Ni^{H}** complex was reported in Chang *et. al*., 2011 and showed two irreversible reduction events at −0.80 V and −1.46 V vs SCE under N_2 atmosphere at the scan rate of 100 mV/s. Under CO_2 atmosphere, the catalytic wave was observed at the second reduction event, which is similar to the other two **Ni^{R}** derivatives mentioned above. The addition of excess water also enhances the current of this second reduction potential.[14]

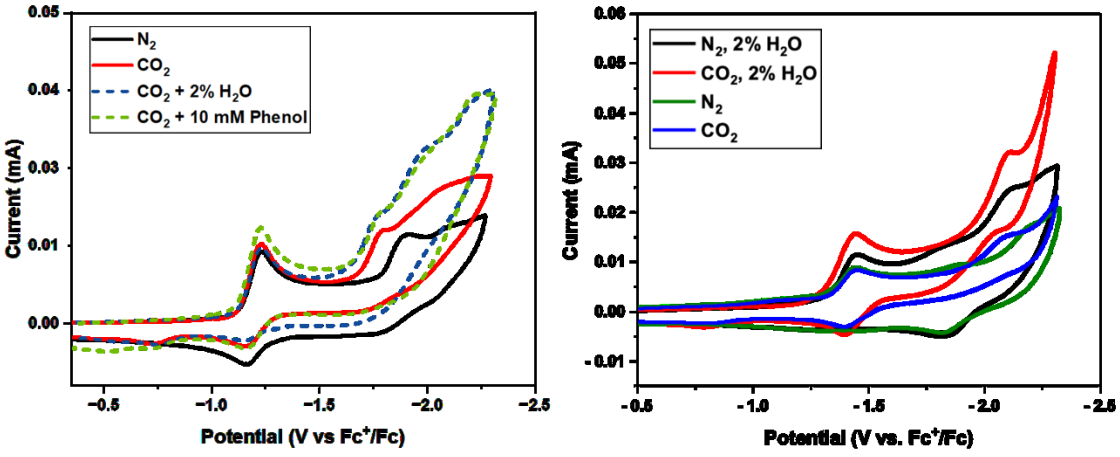

Figure 5: Cyclic voltammograms of **Ni^{OMe}** (left) and **Ni^{OH}** (right) under N_2 and CO_2

The overpotentials for CO and formate were defined as follows. The strongest acid under photocatalytic reaction in acetonitrile is the protonated triethylamine, with the p*K*a value of 18.5,[19] and the standard reduction potential of CO_2 in acetonitrile at −0.12 V vs. Fc^+/Fc,[20] which resulting in the standard reduction potential of CO_2 to CO under photocatalysis reaction condition at −1.21 V vs. Fc^+/Fc.[20, 21] While the standard reduction potential for the conversion of CO_2 to formate under the same condition described above is −1.33 V vs. Fc^+/Fc.[22] The overpotential values of both products are shown in **Table 3**, ranging from −0.40 V to −0.80 V. The onset reduction potential values of **Ni^{OH}** and **Ni^{OMe}** under CO_2 as shown in **Table 3** and **Figure 6** are more positive than that of $Ir(ppy)_3$, −2.61 V, which indicates that $Ir(ppy)_3$ is thermodynamically a suitable photosensitizer used in this photocatalytic CO_2 reduction reaction to activate Ni-NCCN type complexes.[23]

Table 3: Reduction potentials (under N_2 and CO_2) for **Ni^{OH}** and **Ni^{OMe}** complexes (Scan rate = 100 mV/s) and other electrochemical data. Reduction potentials are given against Fc^+/Fc.

Complex	E_{pc1} Peak N_2/CO_2 (V)	E_{pc2} Peak N_2/CO_2 (V)	E_{pc2} Onset N_2/CO_2 (V)	Overpotential for CO (V)	Overpotential for HCO_2^- (V)	i_{cat}/i_p	
						No Proton Source	Proton Source Added
Ni^{OH}	−1.44/−1.45	−2.18/−2.10	−2.13/−2.01	−0.80	−0.68	0.90	1.31
Ni^{OMe}	− 1.23/− 1.23	− 1.93/− 1.79	−1.82/−1.74	−0.53	−0.41	1.15	1.77

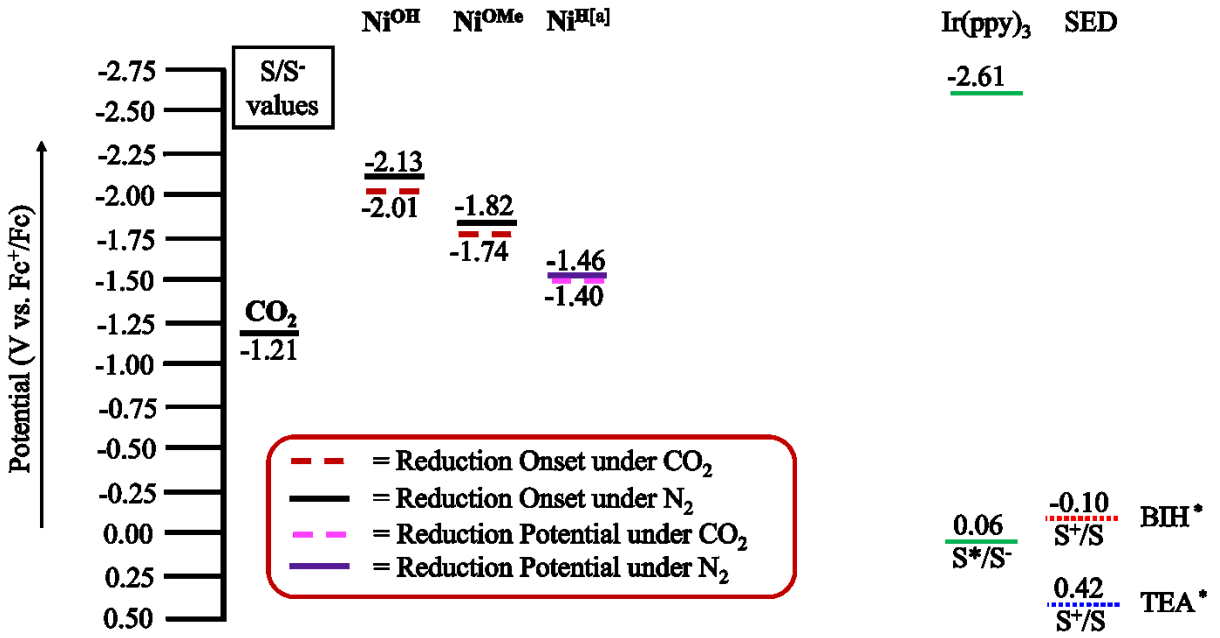

Figure 6: Energy level diagrams based on the onset potential for E_{pc2} of the catalysts (table 3), PS (CV and optical data), and sacrificial electron donors (SEDs) in acetonitrile. Solid lines are estimated reduction onset potentials for E_{pc2} under inert atmosphere, dashed lines are the reduction onset potentials for E_{pc2} under CO2 atmosphere, and short dashes are oxidation potentials. TEA is triethylamine; BIH is 1,3-Dimethyl-2-phenyl-2,3-dihydro-1H-benzimidazole. *BIH and TEA are onset values.[23] [a]These values were estimated from the literature.[14]

Photocatalytic CO_2 Reduction

The four Ni-NCCN type complexes were tested in the photocatalytic CO_2 reduction reaction using $Ir(ppy)_3$ as the photosensitizer (PS) as it has more negative onset reduction potential (-2.61 V vs Fc^+/Fc) compared to the onset reduction potential nickel complexes (**Figure 6**).[23] BIH was also used as a sacrificial electron donor in this reaction due to its strong reducing ability, and triethylamine (TEA) acted as a base to deprotonate the BIH radical cation that formed after the electron transfer to the photosensitizer and thereby promoting an irreversible electron transfer

event.[23] The photocatalytic reactions were done in anhydrous acetonitrile solution containing 1 μM of catalysts concentration, 1×10^{-4} M of $Ir(ppy)_3$, 0.011 M of BIH, and 0.36 M of TEA. The turnover number (TON = moles of product/moles of catalyst) of products (CO and/or formate) was determined at 24 h upon irradiation, while the turnover frequency (TOF = TON/reaction time) of CO was measured at various time points. The CO production was monitored over a period of time using gas chromatography, enabling the determination of TOF of CO in this reaction. The quantification of formate was achieved by analyzing a portion of the reaction mixture after 24 h via ^{1}H NMR spectroscopy. Consequently, it was not feasible to quantify the TOF of formate at earlier time points.

Table 2: Photocatalytic result of CO and formate production by Ni-NCCN type catalysts.[a]

Catalyst	TON_{HCO2}-[b]	TON_{CO}[b]	TOF_I [h^{-1}][c]	TOF_M [h^{-1}][d]	TOF_F [h^{-1}][e]	Φ_{CO} (%)[f]
Ni^{OH}	1803 ± 150	198 ± 20	0	41	8	2.34×10^{-2}
Ni^{OMe}	1880 ± 20	66 ± 8	0	4	3	2.18×10^{-3}
Ni^{OBn}	2300 ± 210	151 ± 10	0	33	6	1.88×10^{-2}
Ni^{H}	2238 ± 70	103 ± 14	0	19	4	1.09×10^{-2}

[a]All experiments were done in triplicate. [b]TON values were measured at 24 h. [c]Initial TOF values are reported at the first 15 minutes for CO production. [d]TOF_{max} values are given for the time point with the fastest rate of reaction for CO production. [e]TOF final was measured at 24 h. [f]The quantum yield (Φ_{CO}) was measured following the procedure in the literature[10]; the maximum TOF for 24 h time period was used in the calculation for each catalyst, and all three catalysts (Ni^{OH}, Ni^{OBn} and Ni^{H}) have max. TOF at 3 h time point, while Ni^{OMe} has max. TOF at 16 h time point.

The main product of photocatalytic CO_2 reduction utilizing these four nickel tetradentate catalysts is formate, with the turnover number varying from ~1800 to ~2300 (**Table 2, Figure 6**). Notably, Ni^{OBn} and the unsubstituted nickel catalyst, Ni^{H}, yielded a greater TON of formate with ~2300, compared to Ni^{OH} and Ni^{OMe} with ~1800 TON. However, the opposite trend observed in

the production of CO, as **Ni^{OH}** has the highest TON of CO compared to the other derivatives, though the TON of CO is still about 9-fold lower than the TON of formate. The initial TOF for each catalyst is zero, suggesting that these are precatalysts that require activation. Similar to the trend for TON_{CO}, catalyst **Ni^{OH}** exhibits the highest maximum and final TOF, with the trend as follow: **Ni^{OH} > Ni^{OBn} > Ni^{H} > Ni^{OMe} (Table 2).** Most of these catalysts exhibit quantum efficiencies (Φ_{CO}) of ~10^{-2} %, except for catalyst **Ni^{OMe}** that has one order of magnitude lower than that of the other three catalysts. Nevertheless, this photocatalytic system is still comparable to the other nickel tetradentate photocatalysts reported in the literature. [9, 10]

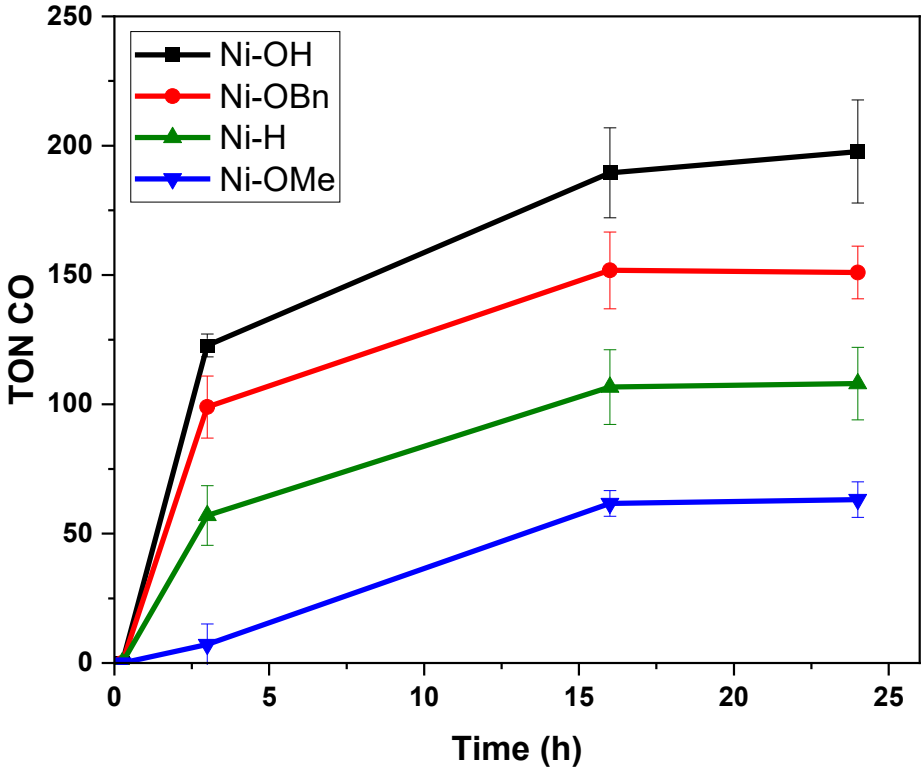

Figure 6: TON vs time plot for the photocatalytic CO_2 reduction to CO with error bars calculated from a standard deviation of three runs of each catalyst.

These four Ni(II) NCCN-type catalysts were further tested for the photocatalytic CO_2 reduction without the presence of photosensitizer, $Ir(ppy)_3$, however, there was only trace amount of formate observed, with no production of CO or other products such as H_2 and CH_4 (**Table S4**). The same results were observed without the addition of BIH for the photocatalytic reaction using catalyst $\mathbf{Ni^{OH}}$ (**Table S4**). The previous studies revealed that the addition of proton source can increase the catalytic activity and product formation.[24-26] Phenol was added to this photocatalytic CO_2 reduction reaction with stoichiometric amount of 3.6 mM using $\mathbf{Ni^{OH}}$ as the catalyst. Surprisingly, the addition of phenol led to a small decrease in TON of both products, with 173 ± 32 for TON CO, and 1293 ± 150 for TON HCO_2^- (**Table S4**). We note that the role of triethylamine (TEA) in this reaction system is to deprotonate the BIH-derived radical cation, and the addition proton source such as phenol may disturb the electron/proton transfer system between the catalyst and BIH/TEA leading to the decrease of products formation.[18] Isotopic labeling study confirms that external CO_2 is the source of CO generated from the photocatalysis CO_2 reduction reaction (**Figure S75-S76**).

Catalyst $\mathbf{Ni^{OH}}$ was used to perform additional experiment to evaluate the potential of nanoparticle formation and catalytic activity of such particle using mercury (Hg^0) test. The mercury (Hg^0) test normally involves the addition of excess Hg^0 once the catalyst gets activated, under efficient stirring, to amalgamate any potential Ni- or Ir-based nanoparticles. If such nanoparticles were catalytically active, there would be a decrease in the catalytic activity.[10, 18, 27, 28] The products of CO_2 reduction reaction such as CO, H_2, CH_4 and HCO_2^- were analyzed upon the addition of Hg^0, and were compared to the results without the addition of mercury (**Figure S75**) Excess Hg^0 (0.5 mL) was added after irradiating $\mathbf{Ni^{OH}}$ for 3 h induction period. Nearly identical photocatalytic activity was observed with and without the addition of Hg^0 (**Figure S75**),

suggesting that this photocatalytic activity is due to a homogenous molecular catalyst and not nanoparticles. [27, 29, 30]

CONCLUSION

In summary, three new Ni complexes bearing NCCN-type ligands have been synthesized and characterized spectroscopically. The electrochemical study has been done for $\mathbf{Ni^{Me}}$ and $\mathbf{Ni^{OH}}$ and it suggested that CO_2 can be activated with the addition of proton source such as water and/or phenol. The photocatalytic CO_2 reduction reaction with these Ni tetradentate catalysts produced formate as the major product with small amount of CO. The unsubstituted $\mathbf{Ni^{H}}$ and $\mathbf{Ni^{OBn}}$ produced the highest amount of formate, while $\mathbf{Ni^{OH}}$ has the highest TON of CO from this reaction.

Experimental Section

General Information. Reactions were prepared and performed under an inert atmosphere (N_2) using glovebox or Schlenk line techniques using oven-dried glassware unless otherwise stated. Work up and purifications were conducted open to air unless otherwise stated. All solvents were dried on a glass contour solvent purification system built by Pure Process Technology, LLC or were used through commercially available dry solvents. All other commercially available reagents were purchased and used without further purification. Literatures procedures were used for the preparation of $\mathbf{1^{OMe}}$ and $\mathbf{Ni^{H}}$. [13, 14, 31]

Instrument and Services. *NMR*: Spectra were recorded in a Bruker AV360 360 MHz, AV500 500 MHz NMR, or Noe 500 MHz cryo-probe spectrophotometer. ^{1}H-NMR chemical shifts were

assigned with respect to the residual peaks from deuterated NMR solvents. *FTIR*: spectra were recorded on a Bruker Alpha ATR-IR spectrophotometer. *MS*: Spectra were obtained in Waters Xevo G2-XS QTOF instrument and Bruker Raplifex instrument. *UV-Vis*: Absorption spectra were recorded in a Jasco V750 Spectrometer using cuvette of 1 cm path length under ambient atmosphere.

Photocatalytic Reaction Setup and Instruments. The photocatalysis experiments were performed by adding nickel catalyst (1×10^{-6} M), $Ir(ppy)_3$ (1×10^{-4} M if present), BIH (0.02 mmol), and triethylamine (5% solvent volume) in the total volume of 2.0 mL (1.9 mL of MeCN and 0.1 mL of triethylamine). Before adding triethylamine, the reaction mixture was diluted with MeCN to 4 mL of a total volume of 20.794 mL in a pyrex test tube with a stir bar. The test tube was sealed with a septum and a screw cap, and the mixture was vigorously degassed by purging CO_2 through the solvent with a long needle until the solvent volume was reduced to 1.9 mL. The anhydrous triethylamine (0.1 mL) was injected to the reaction mixture. The septum was sealed with Teflon tape.

A neutral white LED (Thorlabs: MNWHL4; color temperature 4900 K) with a collimation adaptor (Thorlabs; SM2F32-A) and the lens (Thorlabs: ACL50832U-A) was used for the irradiation of all of the experiments. The reaction was placed at the distance equivalent to 1 Sun of power from 380 – 750 nm (180 mW directly observed or 63.6 mW/cm^2 adjusted for the reported detector area) by measurement with a power meter (COHERENT PowerMax PM10 detector on a FieldMate (1098297) instrument) as determined with a AM 1.5G solar simulator (ScienceTech: SF-300-A: AAA rated collimated solar simulator) with appropriate cut-on/cut-off filters. The headspace analysis was performed with an Agilent 8890 gas chromatography system with a dual detection

system (FID and TCD) with a methanizer and a Porpack Q 6ft, 1/8 in. O.D. column. The injections were done with a VICI gas tight syringe with an airtight stopcock. Formate analysis and evaluation was performed following the procedure in the literature. [18, 23]

SC-XRD Structure Determination Statements. CCDC Deposition Numbers 2235207- 2235209 for $\mathbf{Ni^{Me}}$, $\mathbf{Ni^{Bn}}$ and $\mathbf{Ni^{OH}}$ contain the supplementary crystallographic data for this paper. These data are provided free of charge by the joint Cambridge Crystallographic Data Centre and Fachinformationszentrum Karlsruhe Access Structures service www.ccdc.cam.ac.uk/structures. A suitable single crystal of $\mathbf{Ni^{Me}}$, $\mathbf{Ni^{Bn}}$ and $\mathbf{Ni^{OH}}$ were selected and mounted on a MiTeGen cryoloop in a random orientation on a XtaLAB Synergy R, DW system, HyPix diffractometer. The crystals were kept around 99.97(19) K for $\mathbf{Ni^{Me}}$, 100.01(11) K for $\mathbf{Ni^{Bn}}$ and 100.00(8) for $\mathbf{Ni^{OH}}$ during data collection. The structures were solved with the ShelXT 2014/5[32] solution program using dual methods and Olex 2 1.3-alpha[33] as the graphical interface. The models were refined with ShelXL[34] 2016/6 using full matrix least squares minimization on F^2. All non-hydrogen atoms were refined anisotropically. Hydrogen atom positions were calculated geometrically and refined using the riding model. Data reduction, scaling and absorption corrections were performed using CrysAlisPro 1.171.40.60a. [35] Numerical absorption correction based on gaussian integration over a multifaceted crystal model and empirical absorption correction using spherical harmonics were performed as implemented in SCALE3 ABSPACK scaling algorithm. [36]

Synthesis and Characterization.

Synthesis of $\mathbf{1^{OBn}}$. In an oven-dried reaction flask, sodium hydride (0.327 g, 13.6 mmol), 8 mL of *N,N*-dimethylformamide (DMF), and benzyl alcohol (1.320 mL, 12.74 mmol) were loaded

(**Scheme 1**). Once the effervescence ceased and the solution became clear, 2,6-difluoropyridine (1.00 mL, 11 mmol) was added dropwise while stirring vigorously. The solution congeals briefly and is stirred continuously for 2 h. In a separate reaction flask, 12 mL of DMF and sodium hydride (0.308 g, 12.8 mmol) were loaded and stirred vigorously while adding imidazole (0.866 g, 12.73 mmol) to the solution. The reaction mixture was stirred for 30 min, then this mixture was transferred to previously prepared solution of 2-fluoro-4-benzyloxy pyridine via cannula transfer. The combined solution was heated to 70 ℃ while stirring for 16 h. Then, the reaction was cooled at room temperature and the solvent was removed via rotovap. The dried residue was transferred to separatory funnel with water and extracted with dichloromethane (DCM) 40 mL three times. The DCM layers were dried by rotary evaporation, resulting in a colorless oil. After 16 h of drying a white solid (2.838 g, 0.011 mol, 82%) was obtained. ^{1}H NMR: (360MHz, $CDCl_3$, RT, ppm) δ 8.36 (s, 1H, H_{im}), δ 7.74 (t, ^{3}J = 8.0 Hz, 1H, $H_{p\text{-}py}$), δ 7.62 (t, ^{3}J = 1.4 Hz, 1H, H_{im}), δ 7.52 (bs, 2H, $H_{o\text{-}Bn}$), δ 7.44 (bs, 2H, $H_{m\text{-}Bn}$), δ 7.42 (bs, 1H, $H_{p\text{-}Bn}$), δ 7.24 (t, ^{3}J = 0.9 Hz, 1H, H_{im}), δ 6.95 (d, ^{3}J = 7.7 Hz, 1H, $H_{o\text{-}py}$), δ 6.89 (d, ^{3}J = 8.2 Hz, 1H, $H_{o\text{-}py}$), δ 5.47 (s, 2H, H_{CH2}).

Synthesis of 2^{OMe}. A vial was loaded with 1,3-dibtomopropane (0.1 mL, 0.207 g, 1.035 mmol), 5 mL acetone, and sodium iodide (0.780 g, 5.2 mmol) and the resulting solution was stirred for 24 h at room temperature (**Scheme 1**). Compound $\mathbf{1^{OMe}}$ (0.373 g, 2.13 mmol) and the previously prepared solution were loaded into a pressure tube after celite filtration into the reaction vessel. The pressure tube was sealed and heated to 120 ℃ while stirring for 16 h. Then, the reaction was cooled to room temperature. The white solid that precipitated out of the solution was filtered and rinsed with acetone (0.5392 g, 0.834 mmol, 81% yield). ^{1}H NMR: (360MHz, DMSO, RT, ppm) δ 10.06 (s, 2H, H_{im}), δ 8.60 (s, 2H, H_{im}), δ 8.09 (m, 4H, H_{im} and $H_{p\text{-}py}$), δ 7.57 (d, ^{3}J = 7.5 Hz, 2H, $H_{o\text{-}py}$), δ 7.06 (d, ^{3}J = 8.3 Hz, 2H, $H_{o\text{-}py}$), δ 4.42 (bs, 4H, $H_{N\text{-}CH2}$), δ 3.97 (s, 6H, H_{OMe}), δ 2.62 (quint,

^3J = 6.1 Hz, 2H, $H_{C\text{-}CH2\text{-}C}$). EI-MS ($EI^+$): m/z found (expected): 519.2 ($[C_{21}H_{24}N_6O_2I]^+$, 519.1); 319.3 ($[C_{21}H_{23}N_6O_2]^+$, 391.2)

Synthesis of 2^{OBn}. The synthesis of compound $\mathbf{2^{OBn}}$ followed the procedure for the synthesis of compound $\mathbf{2^{OMe}}$, except $\mathbf{1^{OMe}}$ was replaced with $\mathbf{1^{OBn}}$ (0.691 g, 2.31 mmol) (**Scheme 1**). This procedure resulted in a yellow solid as the product (0.5634 g, 0.7 mmol, 73 % yield). ^{1}H NMR: (360MHz, DMSO, RT, ppm) δ 10.16 (s, 2H, H_{im}), δ 8.64 (s, 2H, H_{im}), δ 8.12 (m, 4H, H_{im} and $H_{p\text{-}py}$), δ 7.62 (d, ^3J = 7.9 Hz, 2H, $H_{o\text{-}py}$), δ 7.50 (d, ^3J = 6.8 Hz, 4H, $H_{o\text{-}Bn}$), δ 7.40 (m, 6H, $H_{m\text{-}Bn}$ and $H_{p\text{-}Bn}$), δ 7.11 (d, ^3J = 8.2 Hz, 2H, $H_{o\text{-}py}$), δ 5.48 (s, 2H, H_{CH2}) δ 4.46 (t, ^3J = 6.6 Hz, 4H, $H_{N\text{-}CH2}$), δ 2.62 (quint, ^3J = 6.8 Hz, 2H, $H_{C\text{-}CH2\text{-}C}$).

Synthesis of 3^{OMe}. Compound $\mathbf{2^{OMe}}$ (0.192 g, 0.298 mmol) was dissolved in 15 mL water, and heated while stirring until the solution became homogenous. A solution of ammonium hexafluorophosphate (0.267 g, 0.164 mmol) in 1 mL water was added dropwise to $\mathbf{2^{OMe}}$ solution (**Scheme 1**). A white precipitate formed immediately, and the mixture was stirred for additional 10 min. The white solid was collected through vacuum filtration and rinsed with water and diethyl ether (0.186 g, 0.272 mmol, 92% yield). ^{1}H NMR: (360MHz, DMSO, RT, ppm) δ 10.01 (s, 2H, H_{im}), δ 8.60 (s, 2H, H_{im}), δ 8.09 (t, ^3J = 7.9 Hz, 2H, $H_{p\text{-}py}$), δ 8.06 (s, 2H, H_{im}), δ 7.56 (d, ^3J = 7.7 Hz, 2H, $H_{o\text{-}py}$), δ 7.07 (d, ^3J = 8.3 Hz, 2H, $H_{o\text{-}py}$), δ 4.42 (t, ^3J = 6.8 Hz, 4H, $H_{N\text{-}CH2}$), δ 3.97 (s, 6H, H_{OMe}), δ 2.60 (quint, ^3J = 6.8 Hz, 2H, $H_{C\text{-}CH2\text{-}C}$). ^{19}F NMR: (339MHz, DMSO, RT, ppm) δ -70.12 (d, $^1J_{P,F}$ = 711.2 Hz, F_{PF6}). TOF-HRMS (ES^+): m/z found (expected): 537.1593 ($[C_{21}H_{24}N_6O_2PF_6]^+$, 537.1603); 391.1868 ($[C_{21}H_{23}N_6O_2]^+$, 391.1882).

Synthesis of 3^{OBn}. The synthesis of compound $\mathbf{3^{OBn}}$ is similar to the procedure to synthesize compound $\mathbf{3^{OMe}}$ (**Scheme 1**), except $\mathbf{2^{OMe}}$ was replaced with $\mathbf{2^{OBn}}$ (0.564 g, 0.707 mmol). This resulting in a white solid as the product (0.511 g, 0.612 mmol, 87 % yield). ^{1}H NMR: (360MHz,

DMSO, RT, ppm) δ 10.09 (s, 2H, H_{im}), δ 8.63 (t, ^3J = 1.6 Hz, 2H, H_{im}), δ 8.10 (m, 4H, H_{im} and $H_{p\text{-}py}$), δ 7.80 (d, ^3J = 7.9 Hz, 2H, $H_{o\text{-}py}$), δ 7.49 (d, ^3J = 6.7 Hz, 4H, $H_{o\text{-}Bn}$), δ 7.40 (m, 6H, $H_{m\text{-}Bn}$ and $H_{p\text{-}Bn}$), δ 7.12 (d, ^3J = 8.2 Hz, 2H, $H_{o\text{-}py}$), δ 5.47 (s, 2H, H_{CH2}) δ 4.42 (t, ^3J = 6.2 Hz, 4H, $H_{N\text{-}CH2}$), δ 2.63 (quint, ^3J = 6.6 Hz, 2H, $H_{C\text{-}CH2\text{-}C}$). TOF-HRMS ($ES^+$): m/z found (expected): 689.2220 ($[C_{33}H_{32}N_6O_2PF_6]^+$, 689.2229); 543.2502 ($[C_{33}H_{31}N_6O_2]^+$, 543.2508).

Synthesis of 4^{OMe}. In an oven-dried reaction flask, compound $\mathbf{3^{OMe}}$ (0.245 g, 0.359 mmol), silver oxide (0.2 g, 0.863 mmol), and 5 mL of acetonitrile were loaded, then concealed from light (**Scheme 1**). The mixture was stirred for 18 h at room temperature, then filtered over celite. Diethyl ether was added to the filtrate while stirring, resulting in white solid precipitate. The solid was collected through vacuum filtration as the product (0.231 g, 0.36 mmol, 82 % yield). ^{1}H NMR: (360MHz, CD_3CN, RT, ppm) δ 7.717 (t, ^3J = 8.0 Hz, 2H, $H_{p\text{-}py}$), δ 7.711 (s, 2H, H_{im}), δ 7.44 (d, ^3J = 1.9 Hz, 2H, H_{im}), δ 7.08 (d, ^3J = 7.7 Hz, 2H, $H_{o\text{-}py}$), δ 6.83 (d, ^3J = 8.2 Hz, 2H, $H_{o\text{-}py}$), δ 4.18 (t, ^3J = 5.4 Hz, 4H, $H_{N\text{-}CH2}$), δ 3.82 (s, 6H, H_{OMe}), δ 2.53 (quint, ^3J = 5.4 Hz, 2H, $H_{C\text{-}CH2\text{-}C}$). TOF-HRMS ($ES^+$): m/z found (expected): 497.0858 ($[AgC_{21}H_{24}N_6O_2]^+$, 497.0855).

Synthesis of 4^{OBn}. The synthesis of compound $\mathbf{4^{OBn}}$ followed the procedure for the synthesis of compound $\mathbf{4^{OMe}}$ (**Scheme 1**), except compound $\mathbf{3^{OMe}}$ was replaced with compound $\mathbf{3^{OBn}}$ (0.305 g, 0.365 mmol). This resulting in white solid as the product (0.278 g, 0.350 mmol, 96% yield). ^{1}H NMR: (360MHz, DMSO, RT, ppm) δ 8.01 (d, ^3J = 2.0 Hz, 2H, H_{im}), δ 7.81 (d, ^3J = 2.0 Hz, 2H, H_{im}), δ 7.78 (t, ^3J = 7.8 Hz, 2H, $H_{p\text{-}py}$), δ 7.35 (m, 10H, $H_{o,m,p\text{-}Bn}$), δ 7.15 (d, ^3J = 7.6 Hz, 2H, $H_{o\text{-}py}$), δ 6.95 (d, ^3J = 8.2 Hz, 2H, $H_{o\text{-}py}$), δ 5.19 (s, 2H, H_{CH2}) δ 3.98 (bs, 4H, $H_{N\text{-}CH2}$), δ 2.42 (bs, 2H, $H_{C\text{-}CH2\text{-}C}$). TOF-HRMS ($ES^+$): m/z found (expected): 649.1479 ($[AgC_{33}H_{30}N_6O_2]^+$, 649.1481).

Synthesis of Ni^{OMe}. In a reaction flask, compound $\mathbf{4^{OMe}}$ (0.102 g, 0.159 mmol), nickel(II) chloride dimethoxyethane adduct (0.042 g, 0.19 mmol), and 3 mL of acetonitrile was added, then the

mixture was concealed from light and stirred for 43 h (**Scheme 1**). This resulting in a dark orange solution and white precipitate. The solution was filtered over celite. To the filtrate, potassium hexafluorophosphate (0.6 g, 0.33 mmol) was added and the mixture was stirred for 16 h. Then the reaction mixture was filtrate over celite again. The filtrate was stirring while adding diethyl ether dropwise, resulting in orange precipitate. The collected orange solid was triturated in boiling ethanol to remove the impurities. The product was recrystallized from ether diffusion into concentrated acetonitrile solution. (0.1059 9, 0.143 mmol, 91% yield). ^{1}H NMR: (360MHz, DMSO, RT, ppm) δ 8.46 (s, 2H, H_{im}), δ 8.48 (t, ^{3}J = 8.1 Hz, 2H, $H_{p\text{-}py}$), δ 7.75 (m, 4H, H_{im} and $H_{o\text{-}py}$), δ 7.22 (d, ^{3}J = 8.5 Hz, 2H, $H_{o\text{-}py}$), δ 4.14 (m, 4H, $H_{N\text{-}CH2}$), δ 3.82 (s, 6H, H_{OMe}), δ 2.15 (bs, 2H, $H_{C\text{-}CH2\text{-}C}$). ^{13}C NMR: (500MHz, DMSO, RT, ppm) δ 166.35 (C_{NCN}), δ 148.69 ($C_{o\text{-}py}$), δ 146.44 ($C_{o\text{-}py}$ and $C_{p\text{-}py}$), δ 126.74 (C_{Im}), δ 118.51 (C_{Im}), δ 106.41 ($C_{m\text{-}py}$), δ 104.06 ($C_{m\text{-}py}$), δ 57.37 (C_{OMe}), δ 45.96 ($C_{N\text{-}CH2}$), δ 30.05 ($C_{C\text{-}CH2\text{-}C}$). ^{19}F NMR: (500MHz, DMSO, RT, ppm) δ -70.10 (d, $^{1}J_{P,F}$ = 713.3 Hz, F_{PF6}). TOF-HRMS (ES^{+}): m/z found (expected): 593.0805 ($[NiC_{21}H_{22}N_6O_2PF_6]^{+}$, 593.0800); 467.1141 ($[NiC_{21}H_{22}N_6O_2F]^{+}$, 467.1142); 447.1075 ($[NiC_{21}H_{21}N_6O_2]^{+}$, 447.1079). TOF-HRMS ($ES^{-}$): m/z found (expected): 144.9655 ($[PF_6]^{-}$, 144.9642).

Synthesis of Ni^{OBn}. The synthesis of **Ni^{OBn}** followed the procedure described for the synthesis of **Ni^{OMe}** (Scheme 1), except **4^{OMe}** was replaced with **4^{OBn}** (0.115 g, 0.144 mmol). After the filtration, the filtrate solution was dried over rotovap, resulting in orange solid as the product. The solid was refluxed in DCM to remove all impurities (0.110 g, 0.123 mmol, 86% yield). ^{1}H NMR: (360MHz, DMSO, RT, ppm) δ 8.44 (d, ^{3}J = 2.0 Hz, 2H, H_{im}), δ 8.08 (t, ^{3}J = 8.1 Hz, 2H, $H_{p\text{-}py}$), δ 7.77 (d, ^{3}J = 2.0 Hz, 2H, H_{im}), δ 7.61 (d, ^{3}J = 8.0 Hz, 2H, $H_{o\text{-}py}$), δ 7.28 (t, ^{3}J = 7.3 Hz, 2H, $H_{p\text{-}Bn}$), δ 7.19 (t, ^{3}J = 7.3 Hz, 4H, $H_{m\text{-}Bn}$), δ 7.08 (d, ^{3}J = 7.1 Hz, 4H, $H_{o\text{-}Bn}$), δ 6.90 (d, ^{3}J = 8.5 Hz, 2H, $H_{o\text{-}py}$), δ 5.14 (bm, 4H, H_{CH2}) δ 4.16 (bm, 4H, $H_{N\text{-}CH2}$), δ 2.13 (bm, 2H, $H_{C\text{-}CH2\text{-}C}$). TOF-HRMS ($ES^{+}$): m/z

found (expected): 745.1424 ($[NiC_{33}H_{30}N_6O_2PF_6]^+$, 745.1426); 619.1763 ($[NiC_{33}H_{30}N_6O_2F]^+$, 619.1768); 599.1696 ($[NiC_{33}H_{29}N_6O_2]^+$, 599.1705); 509.1227 ($[NiC_{26}H_{23}N_6O_2]^+$, 509.1235); 416.1008 ($[NiC_{19}H_{14}N_6O_2]^+$, 416.0532).

Synthesis of Ni^{OH}. In an oven-dried round bottom flask, compound $\mathbf{Ni^{OBn}}$ (0.040 g, 0.045 mmol), 10% Pd/C (0.002 g, 0.0187 mmol) and 5 mL acetonitrile were loaded. The mixture was stirring for 6 hours under H_2 atmosphere (**Scheme 1**). After 6 hours, the mixture was filtered over celite, and the filtrate was dried over rotovap. This resulting in orange solid as the product (0.032 g, 0.056 mmol, 87% yield). ^{1}H NMR: (360MHz, DMSO, RT, ppm) δ 8.32 (s, 2H, H_{im}), δ 7.90 (t, 2H, $H_{p\text{-}py}$), δ 7.67 (s, 2H, H_{im}), δ 7.29 (d, 2H, $H_{m\text{-}py}$), δ 6.70 (d, 2H, $H_{m\text{-}py}$), δ 4.31 (m, 2H, $H_{N\text{-}CH2}$), δ 3.72 (m, 2H, $H_{N\text{-}CH2}$), δ 2.07 (bs, 2H, $H_{C\text{-}CH2\text{-}C}$). ^{19}F NMR: (339MHz, DMSO, RT, ppm) δ -70.10 (d, F_{PF6}). TOF-HRMS (ES^+): m/z found (expected): 419.0767 ($[NiC_{21}H_{22}N_6O_2PF_6]^+$, 419.0765). TOF-HRMS ($ES^-$): m/z found (expected): 144.9643 ($[PF_6]^-$, 144.9642). FT-IR: 3135; 1632; 1478; 827; 554.

Computational Methods

To connect to the UV-Visible absorption spectroscopy experiments, we performed density functional theory (DFT) calculations with Gaussian 16[37]. Using the Conformer-Rotamer Ensemble Sampling Tool[38] (CREST), we determined the most stable conformer of all four synthesized nickel complexes. We retained all conformers within 6 kcal/mol of the most stable conformer at the GFN2-xTB[39] level of theory, following metadynamics simulations of 1.5 fs timestep.[40] We further optimized these conformers at the ωB97X-D(SMD=Acetonitrile)/def2-SVP[41-43] level of theory and selected the lowest energy structure. We verified each stationary point by a normal mode analysis. We then performed time-dependent density functional theory (TD-DFT) and natural

transition orbital (NTO) calculations at the B3LYP-D3(BJ)(SMD=Acetonitrile)/def2-TZVPP[42-47] level of theory to investigate the transition character of the complexes.

Uncategorized References

1. Windle, C. D.; Perutz, R. N., Advances in molecular photocatalytic and electrocatalytic CO2 reduction. *Coordin Chem Rev* **2012,** *256* (21-22), 2562-2570.
2. Benson, E. E.; Kubiak, C. P.; Sathrum, A. J.; Smieja, J. M., Electrocatalytic and homogeneous approaches to conversion of CO 2 to liquid fuels. *Chem Soc Rev* **2008,** *38* (1), 89-99.
3. Kumar, B.; Llorente, M.; Froehlich, J.; Dang, T.; Sathrum, A.; Kubiak, C. P., Photochemical and Photoelectrochemical Reduction of CO2. *Annu Rev Phys Chem* **2012,** *63* (1), 541-569.
4. Izumi, Y., Recent advances in the photocatalytic conversion of carbon dioxide to fuels with water and/or hydrogen using solar energy and beyond. *Coordin Chem Rev* **2013,** *257* (1), 171-186.
5. Su, X.; McCardle, K. M.; Panetier, J. A.; Jurss, J. W., Electrocatalytic CO 2 reduction with nickel complexes supported by tunable bipyridyl-N-heterocyclic carbene donors: understanding redox-active macrocycles. *Chem Commun* **2018,** *54* (27), 3351-3354.
6. Hong, D.; Tsukakoshi, Y.; Kotani, H.; Ishizuka, T.; Kojima, T., Visible-Light-Driven Photocatalytic CO2 Reduction by a Ni(II) Complex Bearing a Bioinspired Tetradentate Ligand for Selective CO Production. *J Am Chem Soc* **2017,** *139* (19), 6538-6541.
7. Concepcion, J. J.; House, R. L.; Papanikolas, J. M.; Meyer, T. J., Chemical approaches to artificial photosynthesis. *Proc National Acad Sci* **2012,** *109* (39), 15560-15564.
8. Finn, C.; Schnittger, S.; Yellowlees, L. J.; Love, J. B., Molecular approaches to the electrochemical reduction of carbon dioxide. *Chem Commun* **2011,** *48* (10), 1392-1399.
9. Thoi, V. S.; Kornienko, N.; Margarit, C. G.; Yang, P.; Chang, C. J., Visible-Light Photoredox Catalysis: Selective Reduction of Carbon Dioxide to Carbon Monoxide by a Nickel N-Heterocyclic Carbene–Isoquinoline Complex. *J Am Chem Soc* **2013,** *135* (38), 14413-14424.
10. Shirley, H.; Su, X.; Sanjanwala, H.; Talukdar, K.; Jurss, J. W.; Delcamp, J. H., Durable Solar-Powered Systems with Ni-Catalysts for Conversion of CO2 or CO to CH4. *J Am Chem Soc* **2019,** *141* (16), 6617-6622.
11. Yao, W.; Olajide, G.; Boudreaux, C. M.; Wysocki, M. M.; Ahmed, M. K.; Qu, F.; Szilvási, T.; Papish, E. T., Cobalt(I) Pincer Complexes as Catalysts for CO2 Hydrogenation to Formate. *Organometallics* **2024,** *43* (13), 1447-1458.
12. Boudreaux, C. M.; Nugegoda, D.; Yao, W.; Le, N.; Frey, N. C.; Li, Q.; Qu, F.; Zeller, M.; Webster, C. E.; Delcamp, J. H.; Papish, E. T., Low-Valent Cobalt(I) CNC Pincer Complexes as Catalysts for Light-Driven Carbon Dioxide Reduction. *ACS Catalysis* **2022,** *12* (14), 8718-8728.
13. Siek, S.; Burks, D. B.; Gerlach, D. L.; Liang, G.; Tesh, J. M.; Thompson, C. R.; Qu, F.; Shankwitz, J. E.; Vasquez, R. M.; Chambers, N.; Szulczewski, G. J.; Grotjahn, D. B.; Webster, C. E.; Papish, E. T., Iridium and Ruthenium Complexes of N-Heterocyclic Carbene- and Pyridinol-Derived Chelates as Catalysts for Aqueous Carbon Dioxide Hydrogenation and Formic Acid Dehydrogenation: The Role of the Alkali Metal. *Organometallics* **2017,** *36* (6), 1091-1106.
14. Thoi, V. S.; Chang, C. J., Nickel N-heterocyclic carbene – pyridine complexes that exhibit selectivity for electrocatalytic reduction of carbon dioxide over water. *Chem Commun* **2011,** *47* (23), 6578-6580.

15. Winter, S. M.; Roberts, R. J.; Mailman, A.; Cvrkalj, K.; Assoud, A.; Oakley, R. T., Thermal conversion of a pyridine -bridged bisdithiazolyl radical to a zwitterionic bisdithiazolopyridone. *Chem Commun* **2010,** *46* (25), 4496-4498.
16. Yang, L.; Powell, D. R.; Houser, R. P., Structural variation in copper(i) complexes with pyridylmethylamide ligands : structural analysis with a new four-coordinate geometry index, τ 4. *Dalton T* **2007,** *0* (9), 955-964.
17. Okuniewski, A.; Rosiak, D.; Chojnacki, J.; Becker, B., Coordination polymers and molecular structures among complexes of mercury(II) halides with selected 1-benzoylthioureas. *Polyhedron* **2015,** *90*, 47-57.
18. Manafe, S. Y.; Le, N.; Lambert, E. C.; Curiac, C.; Nugegoda, D.; Das, S.; Hunt, L. A.; Qu, F.; Whitt, L. M.; Fedin, I.; Hammer, N. I.; Webster, C. E.; Delcamp, J. H.; Papish, E. T., Sensitized and Self-Sensitized Photocatalytic CO 2 Reduction to HCO 2 – and CO under Visible Light with Ni(II) CNC-Pincer Catalysts. *ACS Catal.* **2024**, 6589-6602.
19. Rossini, E.; Bochevarov, A. D.; Knapp, E. W., Empirical Conversion of pKa Values between Different Solvents and Interpretation of the Parameters: Application to Water, Acetonitrile, Dimethyl Sulfoxide, and Methanol. *ACS Omega* **2018,** *3* (2), 1653-1662.
20. Pegis, M. L.; Roberts, J. A. S.; Wasylenko, D. J.; Mader, E. A.; Appel, A. M.; Mayer, J. M., Standard Reduction Potentials for Oxygen and Carbon Dioxide Couples in Acetonitrile and N,N-Dimethylformamide. *Inorg Chem* **2015,** *54* (24), 11883-11888.
21. Costentin, C.; Drouet, S.; Robert, M.; Savéant, J.-M., A Local Proton Source Enhances CO2 Electroreduction to CO by a Molecular Fe Catalyst. *Science* **2012,** *338* (6103), 90-94.
22. Waldie, K. M.; Ostericher, A. L.; Reineke, M. H.; Sasayama, A. F.; Kubiak, C. P., Hydricity of Transition-Metal Hydrides: Thermodynamic Considerations for CO2 Reduction. *ACS Catal.* **2018,** *8* (2), 1313-1324.
23. Rodrigues, R. R.; Boudreaux, C. M.; Papish, E. T.; Delcamp, J. H., Photocatalytic Reduction of CO2 to CO and Formate: Do Reaction Conditions or Ruthenium Catalysts Control Product Selectivity? *Acs Appl Energy Mater* **2019,** *2* (1), 37-46.
24. Liyanage, N. P.; Dulaney, H. A.; Huckaba, A. J.; Jurss, J. W.; Delcamp, J. H., Electrocatalytic Reduction of CO2 to CO With Re-Pyridyl-NHCs: Proton Source Influence on Rates and Product Selectivities. *Inorg Chem* **2016,** *55* (12), 6085-6094.
25. Torre, P. D. L.; Derrick, J. S.; Snider, A.; Smith, P. T.; Loipersberger, M.; Head-Gordon, M.; Chang, C. J., Exchange Coupling Determines Metal-Dependent Efficiency for Iron- and Cobalt-Catalyzed Photochemical CO2 Reduction. *ACS Catal.* **2022,** *12* (14), 8484-8493.
26. Shimoda, T.; Morishima, T.; Kodama, K.; Hirose, T.; Polyansky, D. E.; Manbeck, G. F.; Muckerman, J. T.; Fujita, E., Photocatalytic CO2 Reduction by Trigonal-Bipyramidal Cobalt(II) Polypyridyl Complexes: The Nature of Cobalt(I) and Cobalt(0) Complexes upon Their Reactions with CO2, CO, or Proton. *Inorg Chem* **2018,** *57* (9), 5486-5498.
27. Artero, V.; Fontecave, M., Solar fuels generation and molecular systems: is it homogeneous or heterogeneous catalysis? *Chem Soc Rev* **2013,** *42* (6), 2338-2356.
28. Silprakob W, F. J., Das S, Qu F, Jurss J, Papish E., Synthesis, Characterization, and Catalytic CO2 Reduction Reactivity of Ruthenium CNC Pincer Complexes Containing Macrocyclic or Long Chain Wingtips *ChemRxiv* **2024**.
29. Widegren, J. A.; Finke, R. G., A review of the problem of distinguishing true homogeneous catalysis from soluble or other metal-particle heterogeneous catalysis under reducing conditions. *Journal of Molecular Catalysis A: Chemical* **2003,** *198* (1), 317-341.

30. Crabtree, R. H., Resolving Heterogeneity Problems and Impurity Artifacts in Operationally Homogeneous Transition Metal Catalysts. *Chem. Rev.* **2012,** *112* (3), 1536-1554.
31. Zhu, L.; Guo, P.; Li, G.; Lan, J.; Xie, R.; You, J., Simple Copper Salt-Catalyzed N-Arylation of Nitrogen-Containing Heterocycles with Aryl and Heteroaryl Halides. *The Journal of Organic Chemistry* **2007,** *72* (22), 8535-8538.
32. Sheldrick, G. M., SHELXT-Integrated Space-Group and Crystal-Structure Determination. *Acta Crystallographica Section A* **2015,** *71*, 3-8.
33. Dolomanov, O. V.; Bourhis, L. J.; Gildea, R. J.; Howard, J. A. K.; Puschmann, H., OLEX2: A Complete Structure Solution, Refinement and Analysis Program. *Journal of Applied Crystallography* **2009,** *42*, 339-341.
34. Sheldrick, G. M., Crystal structure refinement with SHELXL. *Structural Chemistry* **2014,** *71*, 3-8.
35. CrysAlisPro *Rigaku Oxford Diffraction*, V1.171.40.80a; 2020.
36. ABSPACK, S. *A Rigaku Oxford Diffraction program for Absorption Corrections, Rigaku Oxford Diffraction*, 2017.
37. Frisch, M. J. T., G. W.; Schlegel, H. B.; Scuseria, G. E.; Robb, M. A.; Cheeseman, J. R.; Scalmani, G.; Barone, V.; Petersson, G. A.; Nakatsuji, H.; Li, X.; Caricato, M.; Marenich, A. V.; Bloino, J.; Janesko, B. G.; Gomperts, R.; Mennucci, B.; Hratchian, H. P.; Ortiz, J. V.; Izmaylov, A. F.; Sonnenberg, J. L.; Williams; Ding, F.; Lipparini, F.; Egidi, F.; Goings, J.; Peng, B.; Petrone, A.; Henderson, T.; Ranasinghe, D.; Zakrzewski, V. G.; Gao, J.; Rega, N.; Zheng, G.; Liang, W.; Hada, M.; Ehara, M.; Toyota, K.; Fukuda, R.; Hasegawa, J.; Ishida, M.; Nakajima, T.; Honda, Y.; Kitao, O.; Nakai, H.; Vreven, T.; Throssell, K.; Montgomery Jr., J. A.; Peralta, J. E.; Ogliaro, F.; Bearpark, M. J.; Heyd, J. J.; Brothers, E. N.; Kudin, K. N.; Staroverov, V. N.; Keith, T. A.; Kobayashi, R.; Normand, J.; Raghavachari, K.; Rendell, A. P.; Burant, J. C.; Iyengar, S. S.; Tomasi, J.; Cossi, M.; Millam, J. M.; Klene, M.; Adamo, C.; Cammi, R.; Ochterski, J. W.; Martin, R. L.; Morokuma, K.; Farkas, O.; Foresman, J. B.; Fox, D. J., Gaussian 16 Rev. C.01. *Wallingford, CT,* **2016**.
38. Pracht, P.; Bohle, F.; Grimme, S., Automated exploration of the low-energy chemical space with fast quantum chemical methods. *Physical Chemistry Chemical Physics* **2020,** *22* (14), 7169-7192.
39. Bannwarth, C.; Ehlert, S.; Grimme, S., GFN2-xTB—An Accurate and Broadly Parametrized Self-Consistent Tight-Binding Quantum Chemical Method with Multipole Electrostatics and Density-Dependent Dispersion Contributions. *Journal of Chemical Theory and Computation* **2019,** *15* (3), 1652-1671.
40. Grimme, S., Exploration of chemical compound, conformer, and reaction space with meta-dynamics simulations based on tight-binding quantum chemical calculations. *Journal of chemical theory and computation* **2019,** *15* (5), 2847-2862.
41. Chai, J.-D.; Head-Gordon, M., Long-range corrected hybrid density functionals with damped atom–atom dispersion corrections. *Physical Chemistry Chemical Physics* **2008,** *10* (44), 6615-6620.
42. Weigend, F.; Ahlrichs, R., Balanced basis sets of split valence, triple zeta valence and quadruple zeta valence quality for H to Rn: Design and assessment of accuracy. *Physical Chemistry Chemical Physics* **2005,** *7* (18), 3297-3305.
43. Marenich, A. V.; Cramer, C. J.; Truhlar, D. G., Universal solvation model based on solute electron density and on a continuum model of the solvent defined by the bulk dielectric

constant and atomic surface tensions. *The Journal of Physical Chemistry B* **2009,** *113* (18), 6378-6396.
44. Becke, A., Density-functional thermochemistry. III. The role of exact exchange (1993) J. *Chem. Phys 98*, 5648.
45. Lee, C.; Yang, W.; Parr, R. G., Development of the Colle-Salvetti correlation-energy formula into a functional of the electron density. *Physical review B* **1988,** *37* (2), 785.
46. Grimme, S.; Antony, J.; Ehrlich, S.; Krieg, H., A consistent and accurate ab initio parametrization of density functional dispersion correction (DFT-D) for the 94 elements H-Pu. *The Journal of chemical physics* **2010,** *132* (15).
47. Grimme, S.; Ehrlich, S.; Goerigk, L., Effect of the damping function in dispersion corrected density functional theory. *Journal of computational chemistry* **2011,** *32* (7), 1456-1465.